Development of High Rate Wearable MIMU Tracking System Robust to Magnetic Disturbances and Body Acceleration

Anonymous Submission

Abstract. In this paper we present a wearable high rate MIMU (magnetic-inertial measurement unit) based body tracking system. It is designed using low cost state-of-art hardware and MEMS sensors to reduce errors and improve computational latency. Our system allows for high rate data acquisition and sensor fusion at low power budget. It can be used for range of applications from extreme activity capture and biomechanical analysis to clinical evaluation and ambulatory health monitoring/rehabilitation. The package size of sensing nodes is small, and we use textile wires which make it very flexible. Thus entire system can be easily integrated with body worn suit/pants. Up to 7x nodes can be connected without compromising the maximum sampling frequency (1 KHz), with the possibility to add more nodes using additional bridge stations between nodes. The acquisition rate can be preset from 1 KHz to 100 Hz to suit the application or accuracy requirements. To the best of our knowledge, our inertial motion capture system is the first to offer such high rate output at 1 KHz for multiple nodes. The high rate of inertial data provides intrinsic accuracy to sensor fusion as well as capture high frequency features for clinical diagnostics and biomechanical analysis in ambient settings. The system also runs an embedded sensor fusion algorithm for accurate orientation estimation. We introduce a novel accelerometer and magnetometer measurement correction with adaptive sensor covariance approach in EKF, which makes it robust to both magnetic disturbances and body accelerations. Thus it is well suited for indoor human motion analysis and monitoring highly dynamic motion.

Keywords: Ambient Intelligence, Wearable Sensor Networks, Sensor Fusion

1 Introduction

Body worn magnetic-inertial measurement unit (MIMU) sensors have become an excellent choice for non-invasive human motion capture, biomechanical analysis and body tracking in non-clinical and ambulatory settings. These wearable sensors are used for applications as diverse as neurological deficit assessment, elderly fall detection, rehabilitation exercises, sports performance, posture and gait analysis, and in Virtual-Augmented Reality (VR/AR). Both harness based and wireless IMU nodes are used for human body tracking, however the wireless IMUs suffer from reliability and synchronization issues, need more power and have bigger form factor for individual nodes. On the contrary, flexible harness based IMUs remain a viable option for less invasive (due to low form factor), reliable and high rate body worn systems with very low energy consumption (cf. Xsens harness based MVN Link® vis-à-vis

wireless Awinda® system [1]). Another desirable feature is the inbuilt processing ability of body-worn IMU systems for sensor fusion. These systems are based on low-cost miniaturized MEMS sensors, which are not very accurate and thus require signal preprocessing and sensor fusion. Most commercial systems support limited onboard processing and are able to deliver orientation estimates (obtained from propriety sensor fusion algorithms) in addition to raw sensor data. However, these propriety filters are not very robust to magnetic disturbances and motion induced errors arising out of body accelerations [2]. The sensor fusion approaches reported in past literature which are claimed robust to magnetic disturbances and fast motion, are either computationally intensive, or do not give very satisfactory results except under restricted assumptions [3-5]. More recently, few authors have turned to kinematic chain constraints[6, 7] to dispense with magnetometer data and use only rate gyros/accelerometers, but again this approach does not prevent orientation drift in the long run.

Thus body accelerations and magnetic disturbance induced artifacts remain the main issue to be resolved for reliable and robust orientation estimation using low cost MIMUs in various ambulatory settings. The pace of evolution and improvement in MEMS sensors is very fast. Better magnetometers, rate gyros and accelerometer are becoming available, driven by needs of personal mobile devices and ubiquitous computing. The rate of adoption of new sensor in MIMU based body tracking and monitoring systems is however not as fast. The primary reason is perhaps the redesign overhead. Nevertheless hardware improvements with better algorithms can lead to state-of-art results. Since the new MEMS based inertial sensors offer much higher sampling rates at less noise/power and give more precise readings, this feature can be used advantageously in both sensor preprocessing and sensor fusion algorithms to achieve higher accuracy. Also data acquisition at high rate is essential to capture fast motion dynamics accurately during extreme activity and/or biomechanical analysis, for example in sports. Some high frequency features in tremors and body seizures may also be crucial to investigate neuromuscular anomalies, which need sampling rates higher than customary 100-120 Hz. At present, wireless based MIMU systems due to their inherent limitations do not offer high rate of data acquisition. In fact the rate of data acquisition from such sensors does not scale very well, as the number of sensors is increased.

In this paper, we present our development of a high rate wearable MIMU based system built using flexible textile harness (all nodes also support optional wireless). Our system offers high rate data acquisition, while estimating orientation through an Extended Kalman Filter (EKF) implemented on embedded hardware with very low latency. Our EKF uses novel accelerometer and magnetometer measurement correction with adaptive sensor covariance approach. The orientation results from individual IMUs in our system are compared with the ground truth orientation obtained from submillimeter accurate OptiTrack® optical motion capturing system. It shows excellent match after hand-eye calibration of two systems. Moreover the orientation estimated using our new EKF is shown to be robust to both soft/hard magnetic disturbances as well as body accelerations.

Although many commercial MIMU based motion tracking systems are available (Xsens MVN, InertialLabs 3DSuit, iSen STT-IBS, Rokoko SmartSuit Pro). Our harness based wearable MIMU system claims low form factor (25x20x5mm) for individual nodes, a Wi-Fi hub based on Intel Edison® module with embedded processing/storage option (up to 1.0 GB), efficient cache management with low latency, good synchronization protocol with a flexible I^2C bus and a low power consumption. Additionally, we describe our improved prototype MIMU system with low noise sensors and ultra-low power consumption, which achieves state-of-art sampling rate (1 KHz for each of 7x IMU nodes) and provide tradeoff between high sampling rates vs. low power consumption, in various application settings. Each IMU node in this new implementation also supports Bluetooth Low Energy (BLE) protocol and can run on-chip code for modest pre-processing and orientation estimation directly. Hence the need of flexible harness/Wi-Fi module is optional.

2 Design and Prototyping

2.1 Hardware Design

The design of our harness based IMU motion tracking system has partly developed and matured as a "meta-product" under collaborative Easy-IMP project supported by European Union Grant No. (*anonymized*). The aim has been '*to develop a lightweight and low form factor MIMU based motion tracking system for ambulatory and non-clinical settings, with low power consumption, decent embedded processing power as well as sufficient on-board storage'*. Intel Edison® platform is selected as the hub for being low-power, low-cost solution with embedded processing ability and on-board storage.

The sensing nodes are based on Invensense® MPU-9150, integrated 9-axis Motion Tracking device that combines a 3-axis MEMS gyroscope, a 3-axis MEMS accelerometer, a 3-axis MEMS magnetometer and a Digital Motion Processor™. This MPU has external triggering option, which makes it extremely useful when combining multiple sensor units. NXP PCA9501 EPROM module has been added to store calibration data of each node, thus calibration information stays on plug-in sensor node. The data transmission happens through a differential I^2C bus connected to the microcontroller of the Edison development board. Differential I^2C bus can run up to 400 KHz, while data acquisition from the 7x IMU sensors take place at 100 Hz sampling rate in this baseline system. The flexible textile wires are used for both power and communication between hub and sensor nodes. Figure 1 shows the Intel Edison® hub connected with textile differential I^2C wire to 7x sensor nodes as well as with textile micro USB wire to the 5V power bank.

The package size of miniaturized sensing nodes is 25x20x5mm, making the system almost non-invasive (Xsens MTw wireless series has IMU size of 47x30x13mm [1]). The flexible textile harness allows easy routing and differential I^2C bus/external trigger of MPU-9150 provides very good synchronization. There is

sufficient free memory/cache (up to 1.0 GB) on Intel Edison module to record an outdoor session. The low current consumption feature of the system is tested with 7x IMU nodes at 100 Hz sampling rate and its current consumption was found out to be 300mA, running raw data calibration, sensor fusion algorithm for all 7x nodes and TCP data transfer on Wi-Fi. This system has been reliably tested for lower body tracking with 7x IMUs and is extendable up to 10 sensors with existing hardware design. Two such sub-systems with synchronization are used for simultaneous upper and lower body tracking.

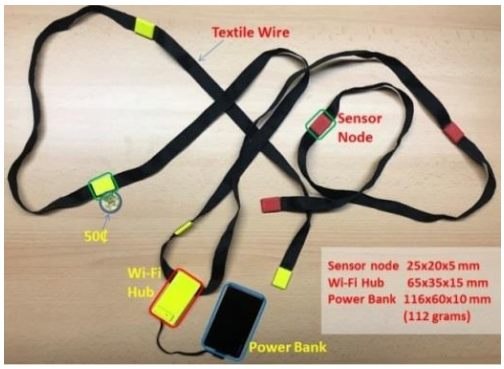

Figure 1: Complete Flexible Harness based MIMU Tracking System

2.2 Plugin Software Architecture

The system has been built with plug-in software architecture in consideration, as shown in Figure 2.

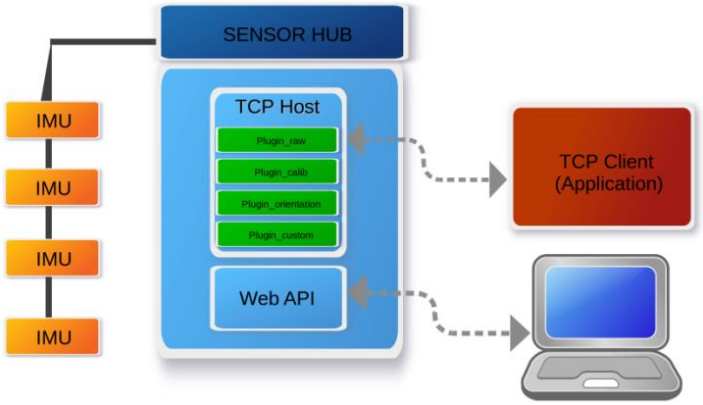

Figure 2: Plugin Software Architecture

Intel Edison® platform runs Yocto Linux. The application can be extended with user compiled code at runtime via a dynamically linked shared library plugin interface.

The definition of the plugin interface and all the application specific API calls are stored on the device itself. The plugins can be activated via generic protocol on the TCP socket. Various types of data are transmitted to the application layer through Wi-Fi (or USB Ethernet) using TCP protocol. The firmware/software framework gathers the sensor data and runs data calibration/fusion algorithm for orientation estimation. It is written in C++ and can be compiled for different platforms with the GNU Compiler. The firmware is set to run on Edison® module as soon as it is accessed by Web API for host application. Both the raw sensor data and orientation estimation from all IMU nodes are available over Wi-Fi.

2.3 Improved Hardware

In sensor fusion and body tracking it is always required to improve the quality of the data delivered by the sensors, in order to implement more accurate tracking. Therefore we evolved our design to a new hardware platform using newer MEMS sensors with better performance in terms of noise levels and bias stability. This new design also offers us flexibility of choosing between wireless and wired communication.

The new prototype for the sensor node design is based on the nRF52832 System on Chip (SoC) that combines an ARM Cortex-M4F microprocessor with a 2.4GHz multi-protocol radio supporting Bluetooth Low Energy (BLE) and ANT multicast protocol. The presence of a low power microcontroller in every node provides the possibility to perform local data preprocessing, thus decreasing the computational load on the hub as well as save on intra-system communication bandwidth.

On every node, there is an ICM20602 6-axis MotionTracking device that combines a 3-axis gyroscope and 3-axis accelerometer in a small 3x3x0.75mm package. The node also contains the MMC3416PJ ultra small 1.6x 1.6x0.6mm, 3-axis magnetic sensor. The nRF52832 SoC communicates through SPI and I^2C with the ICM20602 and MMC3416PJ, respectively. The sampling rate of the system is 1 KHz for the accelerometer and gyroscope, and 500 Hz for the magnetic sensor.

This high sampling rate allows to perform more accurate computations and motion analysis, since more data is available per unit of time, making the system able of capturing fast movements, or to apply preprocessing at node level to increase the measurement accuracy and decrease intrinsic noise level.

The system offers a trade-off between high sample rate and low power consumption, depending on the application and accuracy required, as depicted in Table 1 (the hub performs streaming over Wi-Fi for this budget as well).

TABLE 1: NEW PROTOTYPE- CURRENT CONSUMPTION @ 3.3V

Sampling Frequency	Node Current Consumption	Hub Current Consumption
Idle*	3.8mA	60mA
60 Hz	4mA	100mA
100 Hz	4.2mA	110mA
500 Hz	4.65mA	125mA
1000Hz	6.7mA	140mA

*The idle state occurs when Hub is waiting for the start of a TCP transmission on Wi-Fi.

The improvement in the performance by the new sensors used in this prototype can be observed on Figure 3, where the Allan Variances of the gyroscope and accelerometer are plotted for each axis of the MPU9150 (old inertial sensors) and the ICM20602 (new inertial sensors). It can be observed from the plot that the bias stability of the new sensors (both gyro and accelerometer) is considerably enhanced and intrinsic noise baseline is reduced for new accelerometers.

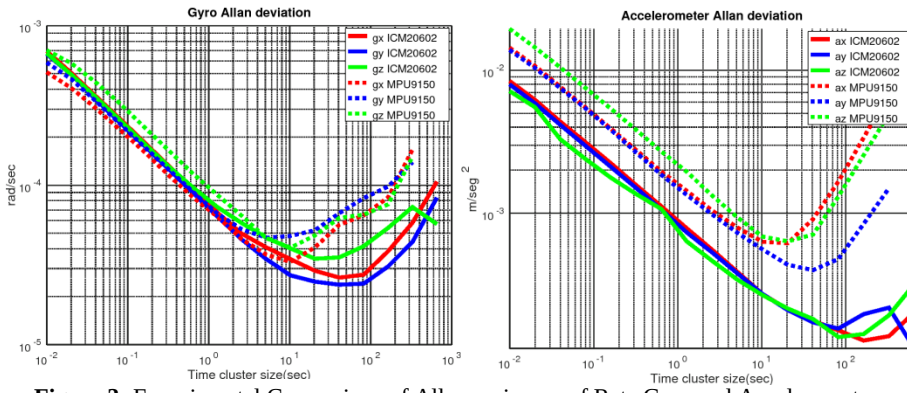

Figure 3: Experimental Comparison of Allen variances of Rate Gyro and Accelerometer used in our Baseline (MPU9150) and Improved System (ICM20602)

The PCB size (Figure 4) of the sensor node for the new prototype is *25.5x18x1.5mm*, including a coaxial antenna connector for possible BLE implementations. The packaging for prototype system is in progress.

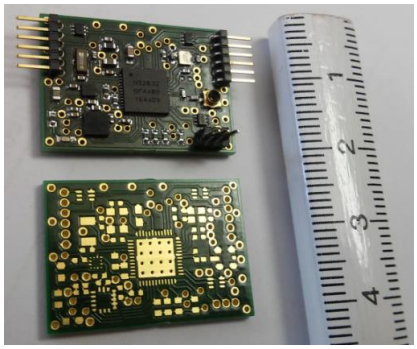

Figure 4: Improved Sensor Node based on nRF52832 System on Chip (SoC) and ICM20602 Motion Tracking

The communication between the new nodes is implemented through textile wires using a 4Mbps SPI Daisy chain protocol. The synchronization is handled by sending a sync signal to every node. Up to 7x nodes can be connected without compromising

the maximum output frequency (1 KHz), with the possibility to add more nodes using additional bridge stations between nodes. For comparison, Xsen harness based MVN Link® offer a maximum output rate of 240 Hz (while internal update rate is 1000 Hz) [1].

The advantage of the new prototype hardware is that it can be adapted to a wide range of possibilities, those that demand the highest output rate can be implemented with the Daisy chain SPI solution using textile harness. On the other hand, the applications that tolerate lower output frequencies can be implemented with the BLE capability that the nRF52832 offers, eliminating the need of Wi-Fi hub, hence decreasing the overall system current consumption (see column 3 in Table 1).

3 Body Integration

The advantage of using textile wires for both data and power sharing is that the system can be conveniently integrated with body worn suit (upper body) and/or pants (lower body) as shown in Figure 5. Enough length of flexible wire between sensor nodes located on different body parts, allows it to stretch and twist while staying integrated with body-fit suit/pant made of stretchable fabric. Thus any maneuver or extreme activity can be performed without hindrance. The weight of nodes and hub is almost negligible and a small weight contribution comes from battery pack itself.

Figure 5: Body Integration of MIMU Motion Capture System

4 Embedded Sensor Fusion

4.1 Sensors Modelling

Inertial sensors such as accelerometers and rate gyros do not measure the quantities of interest only. The measurement of accelerometer has both a constant acceleration due to gravity component as well as acceleration arising from self-motion. Similarly rate gyro measurement has a constant term due to earth rotation. However in case of low cost MEMS rate gyro, this additional term is insignificant and often neglected. In

general for MEMS rate gyro and accelerometer, we can write following Equations relating raw measurements with physical quantities. We follow the convention in this paper that bold small letters represent vectors and bold capital letters are matrices.

$$\boldsymbol{\omega}_{raw} = \boldsymbol{S}^{g}\boldsymbol{\omega} + \boldsymbol{b}_{g} + \boldsymbol{w}_{g} \tag{1}$$

$$\boldsymbol{a}_{raw} = \boldsymbol{S}^{a} \cdot {}^{b}_{n}\boldsymbol{R}\,(\boldsymbol{a} + \boldsymbol{g}) + \boldsymbol{b}_{a} + \boldsymbol{w}_{a} \tag{2}$$

In Equations above, $\boldsymbol{S}$ are 3x3 scaling and misalignment matrices and $\boldsymbol{b}$ are bias terms, while $\boldsymbol{w}$ represent the white Gaussian noise intrinsic to each sensor. ${}^{b}_{n}\boldsymbol{R}$ is a 3x3 rotation matrix that rotate the physical vectors $\boldsymbol{a}$ and $\boldsymbol{g}$ represented in navigation frame of reference to body fixed frame of reference. The vector $\boldsymbol{\omega}$ is the angular rate, while $\boldsymbol{g}$ is the acceleration due to gravity. The body acceleration $\boldsymbol{a}$ (in navigation frame) is often the quantity of interest for navigation purpose. But in orientation and attitude determination problem, body acceleration $\boldsymbol{a}$ represents an undesired disturbance added to reference gravity vector $\boldsymbol{g}$. Similarly we write sensor Equation for magnetometer.

$$\boldsymbol{m}_{raw} = \boldsymbol{S}^{m} \cdot {}^{b}_{n}\boldsymbol{R}\,(\boldsymbol{m}_{n} + \boldsymbol{d}) + \boldsymbol{b}_{m} + \boldsymbol{w}_{m} \tag{3}$$

The difference with inertial sensors is that $\boldsymbol{S}^{m}$ is a 3x3 matrix that in addition to scaling, misalignment and non-orthogonality, also account for soft iron effects. The soft-iron effects are distortions that appear in the measurement due to ferrous materials fixed to body frame. Similarly $\boldsymbol{b}_{m}$ include both the sensor bias as well as hard iron effects due to permanent magnetic sources fixed to body. It is interesting to note that $\boldsymbol{m}_{n}$ - magnetic reference vector for indoor and urban outdoor settings, is often very different from the earth's magnetic field. Also magnetic reference is continuously changed by a position dependent (and slow time varying) disturbance $\boldsymbol{d}$ caused by magnetic sources and ferrous materials present in environment.

4.2 Sensors Calibration

The deterministic errors and effects which are intrinsic to the magnetic and inertial sensors, like scaling, misalignment and non-orthogonality (as well as soft-iron effects) represented by $\boldsymbol{S}$ or biases (and hard iron effects) terms $\boldsymbol{b}$, must be determined in a calibration procedure. In application where quantities of interest are computed by integrating sensor measurements over time, even slight errors in determining $\boldsymbol{S}$ and $\boldsymbol{b}$ can lead to a drift error which increases with time in unbounded fashion. For example, when position is computed from accelerometers or orientation is integrated from rate gyros etc. Thus quality of sensor fusion performed using different sensor modalities is directly dependent on accuracy achieved in intrinsic calibration of sensors. We use a multi-position based procedure [8] for a robust accelerometer calibration. The rate gyros are calibrated using a turn-table procedure, for best accuracy and in order to find precise physical alignment. Thereafter, an in-field quick sensor calibration is carried out before use, in order to fully calibrate magnetometers [9] and update rate gyro biases for any residual errors. These calibration parameters are stored on sensor

node, for later use in sensor fusion. At run-time the calibrated readings (in physical units) are obtained for all sensors as follows.

$$\boldsymbol{\omega}_{cal} = \boldsymbol{S}^{g^{-1}}\left(\boldsymbol{\omega}_{raw} - \boldsymbol{b}_g\right) = \boldsymbol{\omega} + \tilde{\boldsymbol{w}}_g \tag{4}$$

$$\boldsymbol{a}_{cal} = \boldsymbol{S}^{a^{-1}}(\boldsymbol{a}_{raw} - \boldsymbol{b}_a) = {}^{b}_{n}\boldsymbol{R}\,(\boldsymbol{a} + \boldsymbol{g}) + \tilde{\boldsymbol{w}}_a \tag{5}$$

$$\boldsymbol{m}_{cal} = \boldsymbol{S}^{m^{-1}}(\boldsymbol{m}_{raw} - \boldsymbol{b}_m) = {}^{b}_{n}\boldsymbol{R}\,(\boldsymbol{m_n} + \boldsymbol{d}) + \tilde{\boldsymbol{w}}_m \tag{6}$$

4.3 Sensor Fusion

Body segment orientation is the primary quantity of interest in human motion capture and biomechanical analysis. The MIMU sensor nodes are attached to rigid body segments and orientation is obtained through sensor fusion. Two known non-collinear global reference vectors (like Earth's gravity and magnetic field) can provide a global reference frame to define a rigid body orientation. Since the accelerometer measures reference gravity vector, it can give absolute tilt (pitch/roll) information w.r.t gravity vector. Similarly horizontal component of a reference magnetic vector $\boldsymbol{m_n}$ can define magnetic north and gives heading (yaw) information. However as evident from Equation 5 and 6 (Left hand side), both these reference vectors in measurements $\boldsymbol{a}_{cal}$ and $\boldsymbol{m}_{cal}$ are affected by disturbance vectors $\boldsymbol{a}$ and $\boldsymbol{d}$ respectively. Thus Equations 5 and 6 even if solved together, do not provide accurate orientation ${}^{b}_{n}\boldsymbol{R}$. On the other hand, Equation 4 shows that angular rate $\boldsymbol{\omega}_{cal}$ does not suffer from any disturbance (if all bias is eliminated). Hence the following rate equation can be integrated over time from a known initial orientation to predict current orientation.

$${}^{b}_{n}\dot{\boldsymbol{R}} = \frac{1}{2}\boldsymbol{\Omega} \cdot {}^{b}_{n}\boldsymbol{R} \tag{7}$$

Here $\boldsymbol{\Omega}$ is a 3x3 skew-symmetric matrix obtained from $\boldsymbol{\omega}$. The discretization of integration based on Equation 7 is however only approximate and hence small error appears at each time step. Even if gyro bias and calibration is accurately known, integration of Gaussian white noise in gyro readings causes a random walk to appear, even under stationary conditions. Bearing these anomalies in mind, the sensor fusion is the preferred approach for orientation estimation from MIMU sensors.

A robust sensor fusion algorithm ensures that the error converges and the system is also robust to outliers i.e. disturbed accelerometer and magnetometer readings are rejected. The results of past algorithms on account of later goal can still be improved, because when the robustness is checked practically in unrestricted ambulatory settings, drift or random walk error in yaw is very common. This is due to the reason that magnetic disturbances unlike body accelerations are of more permanent nature, as humans move indoor.

Extended Kalman Filter (EKF) has been found computationally cost effective for orientation estimation from noisy MIMU or MARG (magnetic, acceleration and rate gyro) sensors, based on sensor fusion. The unit quaternion representation of orientation is widely popular in these EKF implementations [3], as it avoids Gimbal Lock problem and is less memory intensive than rotation matrix or DCM (Direction Cosine Matrix) representation. It is also very convenient to impose unit norm

constraint on a unit quaternion after each step. Our sensor fusion algorithm is also based on a quaternion based EKF formulation. We implement two EKF filters. **EKF#1** is a baseline sensor fusion algorithm without any measurement covariance adaptation. The process and measurement covariance are assumed constant in this implementation. Whereas **EKF#2** demonstrates our novel covariance adaptation scheme as well as a new magnetometer measurement correction. Thus the difference between two implementations is only in the process and measurement covariance, and will be duly highlighted in description below.

Our state at time step *k* is simply $\boldsymbol{X}_k = \boldsymbol{q}_k$, where $\boldsymbol{q}_k$ is a unit quaternion representing orientation at time step *k*. We initialize with an arbitrary orientation state $\boldsymbol{q}_k = [1\ 0\ 0\ 0]$ i.e. body is assumed aligned with reference North-East-Up global frame. The filter converges very fast to true orientation in few times steps. The state covariance $\boldsymbol{P}_0$ is initialized as diagonal matrix of low values. During this initialization period, average local reference vector $\boldsymbol{m_n}$ is computed as $\boldsymbol{m}_{avg} = \bar{\boldsymbol{m}}_{cal}$ for few time steps.

We have not included gyro bias estimation in our state vector to reduce computational overhead. Also in practical considerations, bias estimated online by EKF is dependent on calibration accuracy of other sensors, which is not always guaranteed. In our case we have seen convergence of state to wrong bias estimates, when it is verified with value obtained from a static test. Instead we prefer to carry out a prior in-field calibration of gyro bias through a static test. This way, we are able to estimate residual gyro bias to high accuracy, till noise threshold of our sensors. Since the bias stability of our MEMS gyro is high (Figure 3), it experiences only minor drift over period of hours. The sensor fusion algorithm is robust to take care of it.

We perform the state prediction step using an average of $\boldsymbol{\omega}_{cal}$ readings of last *k-1* and current time step *k*, i.e. $\bar{\boldsymbol{\omega}} = \frac{\mathbf{1}}{\mathbf{2}}(\boldsymbol{\omega}_k + \boldsymbol{\omega}_{k-1})$. This assumes constant angular acceleration (first order integration) model. Taylor's expansion of the integration of quaternion equivalent of Equation 7 then reduces to

$$\widetilde{\boldsymbol{X}}_k = \ \widetilde{\boldsymbol{q}}_k \ = \boldsymbol{q}_{k-1} \oplus \boldsymbol{q}_{\Delta k} \tag{8}$$

Here $\oplus$ represents quaternion multiplication, $\boldsymbol{q}_{\Delta k} = \left[\cos\frac{|\bar{\boldsymbol{\omega}}|}{2}\Delta k\,,\ \sin\frac{|\bar{\boldsymbol{\omega}}|}{2}\Delta k \cdot \left(\frac{\bar{\boldsymbol{\omega}}}{|\bar{\boldsymbol{\omega}}|}\right)\right]$ represents the change in orientation for this time step and $\widetilde{\boldsymbol{q}}_k$ is the current prediction. The state covariance is updated by

$$\boldsymbol{P}_{k|k-1} = \boldsymbol{F}_k \boldsymbol{P}_{k-1} \boldsymbol{F}_k^T + \ \boldsymbol{Q}_k \tag{9}$$

The $\boldsymbol{P}_{k|k-1}$ represent the uncertainty of new prediction. $\boldsymbol{F}_k$ is the Jacobian evaluated for Equation 8 at $\boldsymbol{q}_{k-1}$ and $\boldsymbol{Q}_k$ is the process covariance arising due to uncertainty of prediction step. In our **EKF#2**, we have adapted $\boldsymbol{Q}_k$ in relation to $\|\bar{\boldsymbol{\omega}}\|$ as follows

$$Q_{\mathrm{ii}}^k = \ variance \ + scale * (\mathrm{Max}(|\bar{\boldsymbol{\omega}}| - threshold, 0)) \tag{10}$$

Now, $\boldsymbol{Q}_k = Diag(Q_{\mathrm{ii}}^k)$. The parameters *variance*, *scale* and *threshold* can be set separately for Equation 10 (or later for Equation 12-13, 19-20). Typical values of these parameters are not given here (for propriety reasons), but algorithm is found

robust for a range of these parameters values. In Equation 10, the first term defines a baseline variance due to integration of gyro noise (random walk), while second term defines the uncertainty arising due to calibration and integration errors that scale with $|\bar{\boldsymbol{\omega}}|$ for a known time step. In contrast, **EKF#1** assumes a constant value for process covariance, $\boldsymbol{Q}_k$.

The correction step with measurements is carried out one by one. First the gravity vector in body reference frame is estimated using predicted quaternion for step *k*

$$\boldsymbol{g}_k^p = \tilde{\boldsymbol{q}}_k \oplus \boldsymbol{g} \oplus \tilde{\boldsymbol{q}}_k^* \tag{11}$$

Where $\boldsymbol{q}^*$ represents conjugate quaternion of $\boldsymbol{q}$. Gravity vector is assumed Up i.e. $\boldsymbol{g} = [0\ 0\ 1]$. Now the residual with measured normalized acceleration is obtained,

$\hat{\boldsymbol{a}} = \left(\frac{\boldsymbol{a_{cal}}}{|\boldsymbol{a_{cal}}|}\right)$, $\boldsymbol{y_a} = (\hat{\boldsymbol{a}} - \boldsymbol{g}_k^p)$. Our **EKF#1** implementation always uses a constant value for measurement covariance $\boldsymbol{R}_k^a$, while measurement covariance in our **EKF#2** algorithm is adapted in two different ways

$$R_{\text{ii}}^{\boldsymbol{a},k} = variance + scale * (\text{Max}(\text{abs}(|\boldsymbol{a}_{cal}| - \text{g}_{avg}) - threshold, 0)) \tag{12}$$

$$R_{\text{ii}}^{\boldsymbol{a},k} = variance + scale * (\text{Max}((|\boldsymbol{y_a}|) - threshold, 0)) \tag{13}$$

So as, $\boldsymbol{R}_k^a = Diag(R_{\text{ii}}^{\boldsymbol{a},k})$. **EKF#2** approach uses Equation 12 during initialization /convergence period, thereafter Equation 13 is used. Equation 13 is a novel covariance adaptation proposed in this paper and the motivation is explained as follows. When the body segments experience downward and sideward acceleration together, a situation may arise when norm of acceleration vector is still equal to normal gravity i.e. 9.81 m/s^2, however acceleration vector direction is perturbed by significant sideward component. Therefore $|\boldsymbol{y_a}|$ which defines Euclidean norm between actual and predicted measurements, gives a better estimate of how good is the actual measurement. Since in general predicted measurement is never same as actual, we allow a threshold, in which covariance (uncertainty) of actual measurement is kept constant. Our process of adapting measurement covariance is depicted in Figure 6.

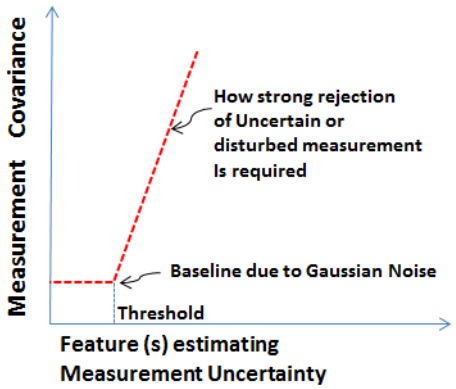

Figure 6: Adaptive Covariance $\boldsymbol{R}_k^a$ and $\boldsymbol{R}_k^m$ for Robust EKF

The innovation $\boldsymbol{S}_k^a$ is now obtained from

$$\boldsymbol{S}_k^a = \boldsymbol{H}_k \boldsymbol{P}_{k|k-1} \boldsymbol{H}_k^T + \boldsymbol{R}_k^a \tag{14}$$

Again $\boldsymbol{H}_k$ is the Jacobian of measurement Equation 11 evaluated at $\widetilde{\boldsymbol{q}}_k$. We get Kalman gain for accelerometer measurement residual, apply error correction to state and update state covariance as follows

$$\boldsymbol{K}_k^a = \boldsymbol{P}_{k|k-1} \boldsymbol{H}_k^T \, (\boldsymbol{S}_k^a)^{-1} \tag{15}$$

$$\boldsymbol{X}_k^a = \widetilde{\boldsymbol{X}}_k + \boldsymbol{K}_k^a \cdot \boldsymbol{y_a} \tag{16}$$

$$\boldsymbol{P}_{k|k}^a = (\boldsymbol{I} - \boldsymbol{K}_k^a \boldsymbol{H}_k^T) \, \boldsymbol{P}_{k|k-1} \tag{17}$$

Since quaternion addition does not respect unit norm constraint, a renormalization after Equation 16 is essential.

While human motion causes only transient acceleration errors to appear in sensing of gravity vector, the sensing of local magnetic field suffers from lot of local variations and sometimes extreme disturbances [2]. Many works have reported success dealing with in particular magnetic disturbances [4, 5, 10]. However, the results reported are often for short durations and obtained by using only rate gyro during periods of magnetometer disturbance. Slight inaccuracies in rate gyro calibration/bias can thus lead to error accumulating over long term, especially indoors. Another approach [11] focuses on modelling, predicting and incorporating magnetic disturbance vector itself. But it is very hard to accurately track magnetic disturbances in the environment. Therefore we have again applied a novel way to deal with it in our **EKF#2** implementation.

In order to remain consistent with other orientation determination algorithms (which assume local magnetic field as North or x-axis), we initialize with magnetic reference vector $\boldsymbol{m}_n = \left[\sqrt{m_x{}^2 + m_y{}^2} \;\; 0 \;\; m_z\right]$, where m_x, m_y, m_z are obtained from $\boldsymbol{m}_{avg}$ initially. We normalize $\boldsymbol{m}_n$ i.e. $\hat{\boldsymbol{m}} = \left(\frac{\boldsymbol{m_n}}{|\boldsymbol{m_n}|}\right)$, then perform measurement update steps in line with equivalent of Equation 11-12 and 14-17 as done for accelerometer measurement, till convergence to initial orientation is achieved in few time steps. Our **EKF#1** implementation then continues with these steps, even after initialization, assuming a constant $\boldsymbol{R}_k^m$. Except after initialization period, we obtain $\boldsymbol{m}_n = \left[\sqrt{m_x{}^2 + m_y{}^2} \;\; 0 \;\; m_z\right]$ at each next step by using m_x, m_y, m_z obtained from ${}_b^n\boldsymbol{R}\, \boldsymbol{m}_{k-1}$, where ${}_b^n\boldsymbol{R} = ({}_n^b\boldsymbol{R})^T$. This step is equivalent to a reset of magnetic reference vector to its best guess at time step *k*.

In our **EKF#2** approach, we eliminate the need to explicitly track or reset the reference magnetic vector using a novel approach. Once initialized, we no longer follow equivalent of measurement Equation 11. Instead we use the fact that change in orientation $\boldsymbol{q}_{\Delta k}$ can rotate the magnetic vector $\boldsymbol{m}_{k-1}$ to $\boldsymbol{m}_k$. Thus our new measurement equation becomes

$$\boldsymbol{m}_k^p = \boldsymbol{q}_{\Delta k} \oplus \boldsymbol{m}_{k-1} \oplus \boldsymbol{q}_{\Delta k}^* \tag{18}$$

Now measurement residual is computed using Equation 18 as $\boldsymbol{y_m} = (\widehat{\boldsymbol{m}} - \boldsymbol{m}_k^p)$. Since $\boldsymbol{m}_{k-1}$ and $\boldsymbol{m}_k$ are disturbed by almost same magnetic disturbance, it is implicitly taken care of. The measurement covariance $\boldsymbol{R}_k^m = Diag(R_{\text{ii}}^{\boldsymbol{m},k})$ is now adapted according to following novel criteria

$$R_{\text{ii}}^{\boldsymbol{a},k} = variance + scale * \Big(\text{Max}\big((|\boldsymbol{y_a}|) - threshold, 0\big)\Big) \quad \text{if } |\bar{\boldsymbol{\omega}}| \leq limit \tag{19}$$

$$R_{\text{ii}}^{\boldsymbol{m},k} = variance + scale * (\text{Max}(\text{abs}(\theta_k^{incl} - \theta_{k-1}^{incl}) - threshold, 0)) \tag{20}$$

where estimate of inclination angle θ^{incl} of local magnetic reference w.r.t gravity is obtained as $\theta_k^{incl} = \cos^{-1}\left(\frac{\boldsymbol{g}_k^p \cdot \bar{\boldsymbol{m}}_{cal}}{\|\boldsymbol{g}_k^p\| \cdot \|\bar{\boldsymbol{m}}_{cal}\|}\right)$. Equation 19 employs same Euclidean norm between actual and predicted measurements as described earlier. However, in case of magnetometer, covariance adaptation using this Equation is only used if $|\bar{\boldsymbol{\omega}}| \leq limit$. At higher $|\bar{\boldsymbol{\omega}}|$, bad magnetometer readings cannot be discriminated from bad predicted measurements using Euclidean norm of residual. Due to gyro calibration errors, higher $|\bar{\boldsymbol{\omega}}|$ lead to more prediction error. Hence, we employ a more robust criteria of checking for good magnetometer readings using inclination angle of $\boldsymbol{m}_{k-1}$ and $\boldsymbol{m}_k$.

After we obtain measurement corrected states $\boldsymbol{X}_k^a$ and $\boldsymbol{X}_k^m$ and corresponding covariance matrices $\boldsymbol{P}_{k|k}^a$ and $\boldsymbol{P}_{k|k}^m$, we simply perform the final fusion step as

$$\boldsymbol{P}_{k|k} = \left((\boldsymbol{P}_{k|k}^a)^{-1} + (\boldsymbol{P}_{k|k}^m)^{-1}\right)^{-1} \tag{21}$$

$$\boldsymbol{X}_{k|k} = \boldsymbol{P}_{k|k}[(\boldsymbol{P}_{k|k}^a)^{-1}\boldsymbol{X}_k^a + \ (\boldsymbol{P}_{k|k}^m)^{-1}\boldsymbol{X}_k^m] \tag{22}$$

The state $\boldsymbol{X_{k|k}}$ obtained from Equation 22 is renormalized to get unit quaternion $\boldsymbol{q_k}$

5 Evaluation Methodology

In our first experiment, we performed evaluation of 1 KHz sampling rate versus 100Hz sampling of our MIMU system to signify the differences and underline the importance of higher rate sampling for highly dynamic body tracking and health monitoring. The data of a single sensor was segmented from 7x sensors data stream which were mounted on a stable platform and moved by right hand of the subject. Various arbitrary gestures with varying speed were performed with intervening rest positions (the platform designed by us allowed for 20 stable rest positions). The stable positions allowed us to segment data of different movement periods (fast versus slow) for analysis.

In second experiment, The real-time results of our EKF#2 implemented on *Edison*® module of IMU tracking system were compared with ground truth obtained from submillimeter accurate OptiTrack® system. The hand-eye calibration for the two systems has been performed using procedure in [12]. The rigid body configuration with placement of optical markers is shown in Figure 7. A single sensor with *Edison*® module was used for this experiment.

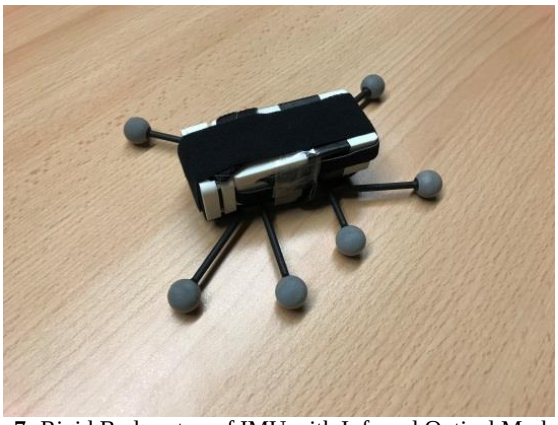

Figure 7: Rigid Body setup of IMU with Infrared Optical Markers for Combined OptiTrack® and IMU Tracking

We initially started from a rest position, carried out first set of sudden movement for computing temporal alignment between two systems. The first set of movements was also employed for hand-eye calibration (spatial frame alignment). Then various set of movements were performed for short-to-moderate durations with intervening rest positions to segment out these movements. The data obtained from two systems (after temporal and spatial frame alignment) were then compared. Both fast and slow movements with different degree of amplitude were performed in this experiment.

In order to evaluate the robustness of our sensor fusion algorithm for orientation estimation against body accelerations and magnetic disturbances, we further performed experiment 3 and 4 respectively. In particular performance of our **EKF#1** (baseline) implementation against **EKF#2** were compared. For experiment 3, we again obtained the data of a single sensor segmented from 7x sensors stream, which was mounted on a stable platform and moved by right hand of the subject. Various arbitrary gestures with varying speed were performed, similar to experiment 1. These movement periods were interjected with static rest positions. The magnitude profile of acceleration during these movements is shown in Figure 13 (Results section). Apart from body vibrations (tremors), significant fast accelerations can be observed to occur during change from one rest position to another in the norm of observed acceleration. We chose intervening rest positions after movement periods, in order that filter response can be easily observed in the plots.

For experiment 4, we chose the same set-up, except now we introduced hard and soft magnetic disturbance. The magnitude profile of these magnetic disturbances is easily observable in Figure 14 (Results section). We introduce these disturbances during rest periods to easily observe the resulting filter behavior. Soft iron disturbances are introduced by bringing in a cubic ferrous block of 5cm×5cm×5cm close to MIMU and are discernible by slight change of magnetic norm in Figure 14. For hard iron disturbances we used stack of small Neodymium magnets with varying strength (by adding to or removing from stack) in the range 100-500μT (our observed ambient indoor field strength was in the range 25-88μT and 25μT is mapped as unit norm in plot). Hard iron disturbance can be observed as sharp spike in Figure 14.

6 Results and Discussion

6.1 Advantage of High Rate Inertial Sensors Data acquisition

The results of our first experiment are depicted in Figure 8 and 9 for accelerometer and rate gyro respectively for 100 Hz and 1000 Hz sample rate. It is important to observe in Figure 8 that the high frequency features present at 1000 Hz are quite under-sampled at 100 Hz in acceleration data.

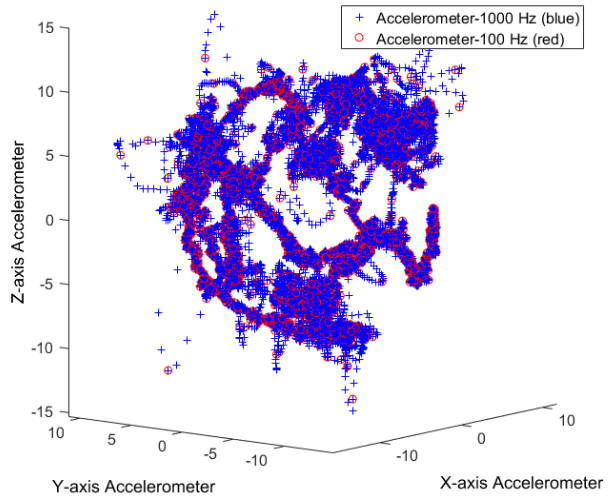

Figure 8: Accelerometer sampling at 100 Hz leads to sparse features in region of fast motion/body tremors etc.

Apparently in Figure 9, rate gyro readings at 100 Hz appear good approximation of trajectory at 1000 Hz. However since in sensor fusion (sub-section 4.3) Equation 10 represents only a first order integration model of Equation 7, we observe that the assumption regarding constant angular acceleration is not valid between two samples of rate gyro measurements at 100Hz. Hence during periods of fast motion, orientation integration error increases.

Since the resulting integration error is cumulative, Equation 10 or any other approximate discrete model for integration of Equation 7 provides better accuracy with higher rate. Even with sensor fusion, during periods (or time steps) of bad magnetometer readings, our heading (yaw) estimates depend largely on rate gyro integration. Unlike gravity, there is no absolute magnetic reference indoors, hence rate gyro integration errors only get accumulated slowly. Thus depending on accuracy and application, we must choose an appropriate rate of data acquisition from accelerometer and rate gyro.

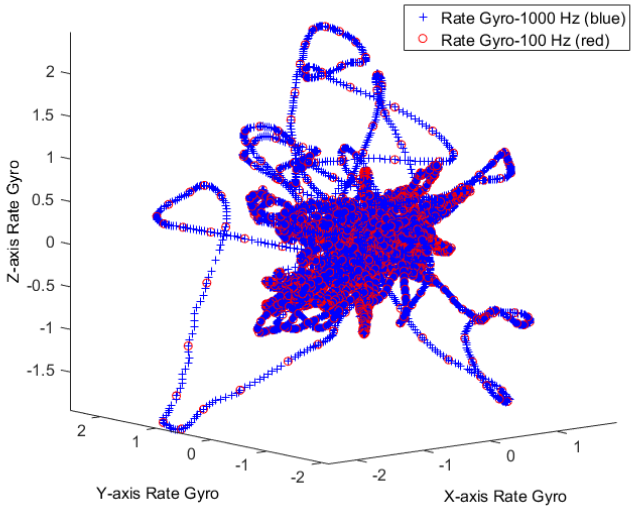

Figure 9: Sampling of rate gyro at 100 Hz, while trajectory at 1000 Hz shows angular acceleration is not constant

6.2 Comparison of IMU tracking with OptiTrack® System

In second experiment, we ran our **EKF#2** implemented on *Edison*® module of IMU tracking system and the ground truth was simultaneously obtained from submillimeter accurate OptiTrack® system. The error in Euler angles w.r.t ground truth over multiple test sequences is summarized in Table 3. It shows that the error increases significantly for fast movements, but 95% of time the error remains in the range of $\pm 5^{o}$. This finding is in agreement with [13] , which reports that accuracy of IMU tracking depends upon both the amplitude and frequency of movement. Our error performance is also better than that reported for Xsens MTw sensors, which only report static and dynamic RMS accuracy instead of 95% range. Xsen MTw series static accuracy for pitch/roll is reported 0.5^{o} RMS and for yaw is 1.0^{o} RMS, dynamic accuracy for pitch/roll is reported 0.75^{o} RMS and for yaw is 1.5^{o} RMS [1]. Compared with Xsen MTw series, we also report our accuracy for high rate dynamic movements of large amplitude (column-3 in Table 2), where filtering performance is crucial.

TABLE 2: ERROR ANALYSIS

	At Rest	***Slow Movements***	***Fast Movements***
Yaw error	±0.01	±0.5	±5
Pitch error	±0.0025	±0.25	±4.25
Roll Error	±0.15	±1.25	±5
@ 100Hz Sampling rate of OptiTrack® and IMU tracking. 95% of errors lie within reported limits			

Figure 10-12 display our results for yaw, pitch and roll angles (ZXY order) tracked via both OptiTrack® and IMU based systems for test duration of 10 min. Only a part of sequence comprising of fast movements (comprising of 70 seconds) is shown for better visualization of amplitude changes. The inset plot in each figure tries to depict the error between two systems more clearly.

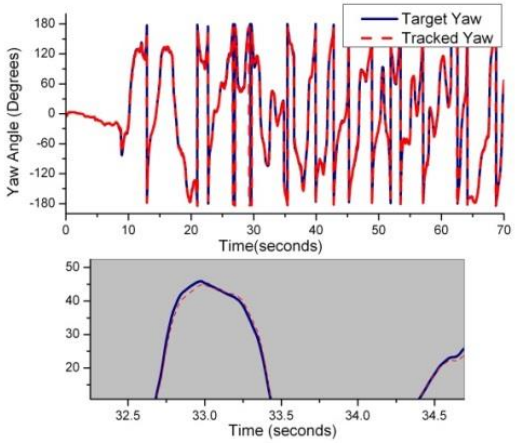

Figure 10: Comparison of OptiTrack® and IMU Tracking (Yaw Angle- ZXY order)

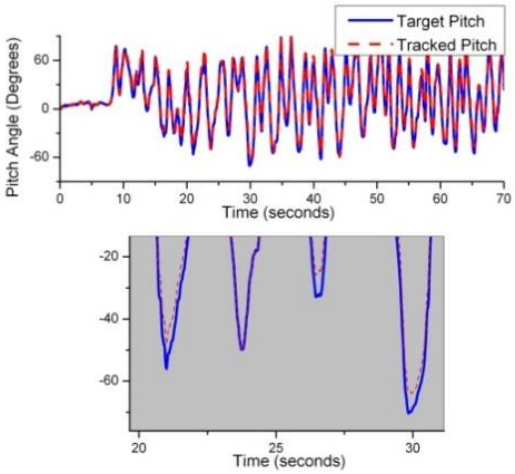

Figure 11: Comparison of OptiTrack® and IMU Tracking (Pitch Angle- ZXY order)

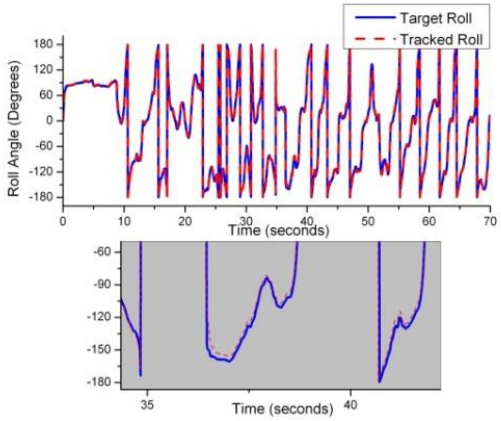

Figure 12: Comparison of OptiTrack® and IMU Tracking
(Roll Angle- ZXY order)

6.3 Robustness against Body Acceleration

The accurate real-time performance of **EKF#2** obtained in experiment 2, lies in strong rejection of acceleration induced errors and magnetic disturbances. It is compared with **EKF#1** algorithm in experiment 3 and 4 to elaborate this feature further. Figure 13 describes the performance comparison of **EKF#2** with **EKF#1** in presence of strong accelerations. Only pitch angle output is shown, as both pitch/roll are affected by the acceleration in a similar manner. Also for ease of visualization, **EKF#1** and **EKF#2** outputs are shown with an offset (these overlap in real). It can be seen that pitch angle output of **EKF#1** is affected by even small accelerations (even due to tremors/vibrations) while that of **EKF#2** is smooth. Also fast convergence of filter algorithm can still be seen despite strong rejection of acceleration, during pitch angle change to new rest position.

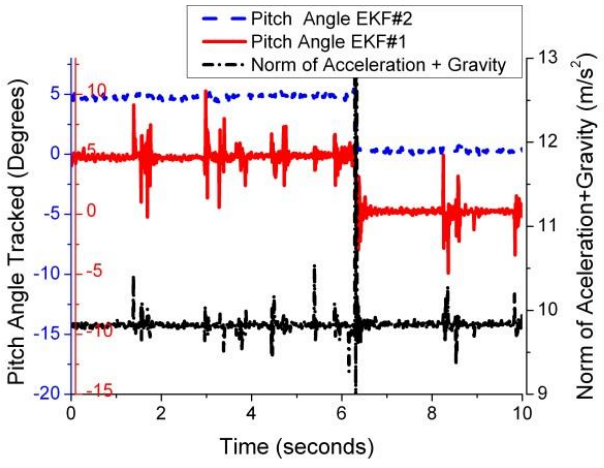

Figure 13: Performance Comparison of **EKF#1** and **#2**
(outputs shown with offset), Rejection of Acceleration Errors

6.4 Performance in presence of Magnetic disturbances

A strong magnetic disturbance was introduced in experiment 4, as shown by changes in the norm of local magnetic field in Figure 14 (soft iron disturbances appear as smaller spikes in norm value, while hard iron disturbance induce a sharp spike in norm of magnetic field). Since the magnetic disturbance predominantly affect the heading (yaw) angle, therefore only a plot of yaw angle is shown. Again for ease of visualization, **EKF#1** and **EKF#2** outputs are shown with an offset (these overlap in real). The yaw angle estimation by **EKF#1** was not robust to these magnetic variations, while **EKF#2** has been shown to be less perturbed, despite magnetic disturbance.

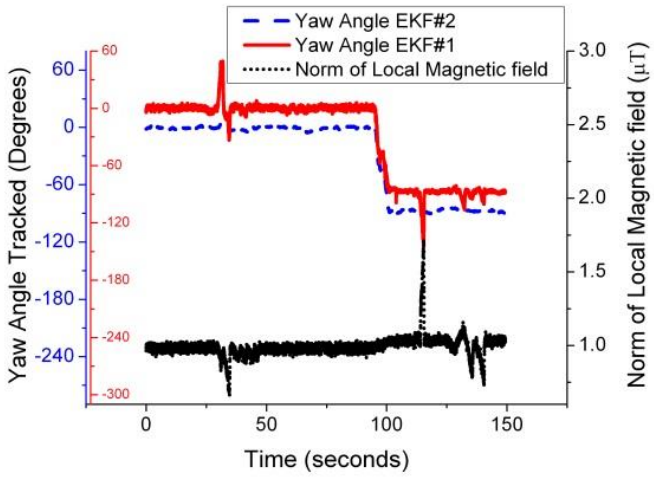

Figure 14: Performance Comparison of **EKF#1** and **#2** (outputs shown with offset), Rejection of Magnetic Disturbances

Experiments were also made with Xsens MTi-28A##G## sensor running propriety XKF sensor fusion using Xsens MT manager. When subjected to same magnetic disturbances, the sensor lost its yaw orientation and drifted to align with direction of new magnetic field. XKF sensor fusion algorithm also shows a constant drift in yaw angle (due to residual gyro bias). The results of two sensor systems are compared in our supplementary video.

7 Conclusion

Using improved hardware, a low power high rate wearable MIMU based body tracking system has been designed to operate at 1 KHz (or lower sampling rates). The system is both non-invasive and ambulatory in view of its small size and onboard data storage. A real-time on-chip EKF robust to body accelerations and magnetic disturbances has been implemented on this embedded system with low computational latency. Our system provides great flexibility of use and is particularly well-suited to capture fast motion dynamics accurately during extreme activity and/or biomechanical applications, especially in indoor settings. The high rate of inertial data

also provides intrinsic accuracy to sensor fusion as well as capture high frequency features for clinical diagnostics and biomechanical analysis in such ambient settings.

References

1. Xsens Homepage, https://www.xsens.com/products/mtw-awinda/, last accessed 2016/11/21.
2. X. Robert-Lachaine, *et al.*, "Effect of local magnetic field disturbances on inertial measurement units accuracy," *Applied Ergonomics*, vol. 63, pp. 123-132 (2017).
3. X. Yun and E. R. Bachmann, "Design, implementation, and experimental results of a quaternion-based Kalman filter for human body motion tracking," *IEEE transactions on Robotics*, vol. 22, pp. 1216-1227 (2006).
4. J.-S. Hu and K.-C. Sun, "A Robust Orientation Estimation Algorithm Using MARG Sensors," *IEEE Transactions on Instrumentation and Measurement*, vol. 64, pp. 815-822 (2015).
5. P. Daponte, *et al.*, "Compensating magnetic disturbances on MARG units by means of a low complexity data fusion algorithm," In: *IEEE International Symposium on Medical Measurements and Applications (MeMeA)*, pp. 157-162 (2015).
6. T. Seel, *et al.*, "Joint axis and position estimation from inertial measurement data by exploiting kinematic constraints," In: *IEEE International Conference on Control Applications (CCA)* , pp. 45-49 (2012).
7. M. Miezal, *et al.*, "A generic approach to inertial tracking of arbitrary kinematic chains," In: *Proceedings of the 8th international conference on body area networks*, pp. 189-192 (2013).
8. S. Poddar, *et al.*, "A comprehensive overview of inertial sensor calibration techniques," *Journal of Dynamic Systems, Measurement, and Control*, vol. 139, p. 011006 (2017).
9. Y. Wu, *et al.*, "Dynamic magnetometer calibration and alignment to inertial sensors by Kalman filtering," *IEEE Transactions on Control Systems Technology*, vol. 26, pp. 716-723 (2018).
10. B. Fan, *et al.*, "An Adaptive Orientation Estimation Method for Magnetic and Inertial Sensors in the Presence of Magnetic Disturbances," *Sensors*, vol. 17, p. 1161 (2017).
11. C.-I. Chesneau, *et al.*, "Improving magneto-inertial attitude and position estimation by means of a magnetic heading observer," In: *International Conference on Indoor Positioning and Indoor Navigation (IPIN)*, pp. 1-8 (2017).
12. M. Pancholi, *et al.*, "Relative Translation and Rotation Calibration Between Optical Target and Inertial Measurement Unit," In: *International Conference on Sensor Systems and Software*, pp. 175-186 (2016).
13. L. Ricci, *et al.*, "On the orientation error of IMU: Investigating static and dynamic accuracy targeting human motion," *PloS one*, vol. 11, p. e0161940 (2016).